Cell Reports
Physical Science

CellPress
OPEN ACCESS

Article

Supercapacitive performance of ionic-liquid-intercalated two-dimensional $Ti_3C_2T_x$ in redox electrolyte

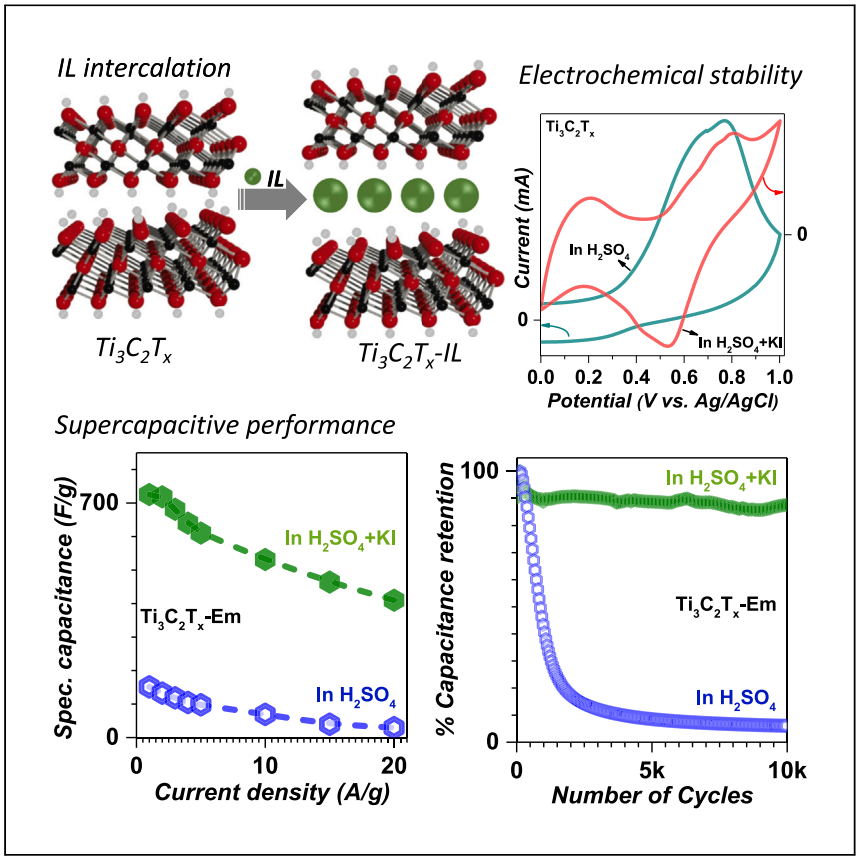

Jadhav et al. show that intercalation of ionic liquids increases the interlayer space of $Ti_3C_2T_x$, which is a suitable candidate for energy storage. A slight variation in the ionic liquids significantly alters charge storage characteristics, and the redox electrolyte prevents the degradation of $Ti_3C_2T_x$-based electrodes in higher anodic potentials while improving capacitance.

Ashwini Jadhav, Plawan Kumar Jha, Mikko Salomäki, Sari Granroth, Pia Damlin, Carita Kvarnström

plawanjha@gmail.com (P.K.J.)
carkva@utu.fi (C.K.)

Highlights

Ionic liquid intercalation increases the interlayer space of 2D-$Ti_3C_2T_x$

Redox electrolyte prevents the degradation of $Ti_3C_2T_x$ in the anodic potential region

Both the ionic liquid and redox electrolyte improves the capacitance of $Ti_3C_2T_x$

Jadhav et al., Cell Reports Physical Science 5, 101788
February 21, 2024
https://doi.org/10.1016/j.xcrp.2024.101788

Cell Reports
Physical Science

CellPress
OPEN ACCESS

Article

Supercapacitive performance of ionic-liquid-intercalated two-dimensional $Ti_3C_2T_x$ in redox electrolyte

Ashwini Jadhav,[1,2] Plawan Kumar Jha,[1,*] Mikko Salomäki,[1] Sari Granroth,[3] Pia Damlin,[1] and Carita Kvarnström[1,4,*]

SUMMARY

Two-dimensional (2D)-$Ti_3C_2T_x$ is a promising candidate for supercapacitors; however, it undergoes irreversible oxidation in aqueous acidic electrolytes at a higher anodic potential. Here, we enhance the supercapacitive performance of $Ti_3C_2T_x$ in the potential range of 0–1 V by a suitable combination of intercalating molecules (for example, $EmBF_4$ [1-ethyl-3-methylimidazolium] and $BmBF_4$ [1-butyl-3-methylimidazolium] tetrafluoroborate) and redox electrolytes (for example, H_2SO_4 plus KI). Pristine $Ti_3C_2T_x$, Em-intercalated $Ti_3C_2T_x$ ($Ti_3C_2T_x$-Em), and Bm-intercalated $Ti_3C_2T_x$ ($Ti_3C_2T_x$-Bm) are utilized for supercapacitor applications and show low capacitance and poor stability in 1 M H_2SO_4. Interestingly, $Ti_3C_2T_x$, $Ti_3C_2T_x$-Em, and $Ti_3C_2T_x$-Bm supercapacitors exhibit improved performance in redox electrolyte. In particular, $Ti_3C_2T_x$-Em demonstrates gravimetric capacitance of 725 Fg^{-1} and >90% capacitance retention after 10,000 cycles. We attribute this high performance to (1) the higher interlayer spacing of $Ti_3C_2T_x$-ionic liquids and (2) effective interaction of the redox pair with the $Ti_3C_2T_x$-Em framework. Our findings suggest that incorporating anodic redox pairs into aqueous acidic electrolytes is a valuable strategy to improve the performance of $Ti_3C_2T_x$ electrodes.

INTRODUCTION

Soaring energy necessity demands extensive study on affordable, environment-friendly, and sustainable electric energy storage devices—supercapacitors and batteries.[1,2] Unlike batteries, supercapacitors possess high power density and long cycle stability; however, lower energy density hinders their broader applications.[3–5] Therefore, continuous development and modification of active electrode materials and electrolytes are essential. In this regard, various carbonaceous and MXene-based materials, metal oxides, and conducting polymers have been explored as electric double-layer capacitors (EDLCs) and pseudocapacitors in symmetric and asymmetric electrode setups.[6–8] In the quest for two-dimensional (2D) materials beyond graphene, MXenes have been determined to be imperative.[9,10] MXenes are 2D transition metal carbides/nitrides synthesized by the etching of A layers from the 3D layered carbides/nitrides known as MAX, where M is a transition metal, X is carbon/nitrogen, and A is a group IIIA or IVA element (Al, Si, Ge). MXenes are represented by the general formula $M_{n+1}X_nT_x$ (n = 1–3), where T_x is the surface-terminating group (i.e., OH, -O, -F, -Cl).[11,12] $Ti_3C_2T_x$ is one of the most explored MXenes for supercapacitors owing to its excellent physicochemical properties.[13–15] Recently, free-standing $Ti_3C_2T_x$ films have shown promising results; however, their

[1]Department of Chemistry, Turku University Centre for Materials and Surfaces (MatSurf), University of Turku, Henrikinkatu 2, 20500 Turku, Finland

[2]University of Turku Graduate School (UTUGS), Doctoral Programme in EXACT Sciences (EXACTUS), Turku, Finland

[3]Department of Physics and Astronomy, University of Turku, 20500 Turku, Finland

[4]Lead contact

*Correspondence: plawanjha@gmail.com (P.K.J.), carkva@utu.fi (C.K.)

https://doi.org/10.1016/j.xcrp.2024.101788

tendency to layer stack undermines their capacitance performance.[16,17] To overcome this limitation, combining $Ti_3C_2T_x$ with metal oxides, carbon-based materials, and conducting polymers appears to be crucial. Moreover, the intercalation of metal cations or other small molecules into $Ti_3C_2T_x$ interlayers is also widely recognized.[18,19] In this line, the first report on intercalation of different cations (Na^+, K^+, Mg^+, NH_4^+, Al^{3+}) in $Ti_3C_2T_x$ demonstrated a change in the c-lattice parameter (increased interlayer space), and its electrochemical measurements in alkaline electrolytes showed a high volumetric capacitance of 350 Fcm^{-3}.[20] Apart from metal cations, numerous organic cations have also been intercalated.[21–23] Among these, the intercalation of room temperature ionic liquids (RTILs) into the $Ti_3C_2T_x$ is on the rise, as it provides additional advantages.[24,25] ILs are considered perfect designer solvents due to numerous physical and chemical properties ascending from different cation-anion combinations. Additionally, they possess high ionic conductivity and thermal stability and have low vapor pressure, making them less toxic than many organic solvents.[26] Imidazolium-based ILs, such as 1-ethyl-3-methylimidazolium ($EmBF_4$) and 1-butyl-3-methylimidazolium tetrafluoroborate ($BmBF_4$) (or $TFSI^-$), are a widely studied group of RTILs. Moreover, IL electrolytes have also shown tremendous potential in supercapacitors, given their stability over a wide electrochemical window.[27] Recent studies have focused on the synthesis of $Ti_3C_2T_x$ films with intercalated RTIL cations, demonstrating promising results for energy storage applications.[28] Furthermore, M. Naguib and co-authors demonstrated that electrodes made from pre-intercalated alkylammonium salt-$Ti_3C_2T_x$ (interlayer space increased from 13.48 to 25.22 Å for $Ti_3C_2T_x$-C16) delivered high capacitance in an EmTFSI electrolyte (neat and in acetonitrile).[23] As most of the studies on MXene-based supercapacitors use it as a negative electrode, Atsuo Yamada and co-workers have emphasized the necessity of developing robust MXene positive electrodes for practical electrochemical energy storage applications.[13]

Aqueous acid electrolytes have been used in supercapacitors for decades because of their high ionic conductivities. However, enhancing the energy density ($E = ½ CV^2$) of materials with lower capacitance values is difficult due to the narrow electrochemical potential window (1.23 V) of water.[29] On the other hand, adding redox molecules/complexes to the electrolytes could significantly enhance the overall capacitance performance of the supercapacitors. Previous studies have shown that both metal-based and metal-free redox entities, such as ferrocene,[30] $Cu(II)Cl_2/SO_4$,[31] $VOSO_4$,[31] $K_2/K_3Fe(CN)_6$,[32] benzoquinone/hydroquinone,[33,34] 1,4 naphthoquinone,[35] thionine,[36] p-phenylenediamine,[33] methyl viologen,[37] and KI,[38] in various aqueous acidic/neutral/basic electrolyte media have elevated the capacitance performance of graphene, conducting polymers, and $Ti_3C_2T_x$-based materials. Due to the fixed electrochemical potential window of $Ti_3C_2T_x$ in aqueous acidic electrolytes, a couple of redox systems were ruled out during selection. Redox pairs, such as I^-/I^{3-} and Fe^{3+}/Fe^{2+}, are active in the higher anodic region where $Ti_3C_2T_x$ undergoes irreversible oxidation and are thus considered unsuitable.[31] However, it is important to note that the iodine redox pairs have a tendency to chemically interact with the organic/inorganic materials, and so they can interact with $Ti_3C_2T_x$ and perhaps suppress the irreversible oxidation. Furthermore, the introduction of iodine redox pairs in aqueous acid electrolytes will not only increase the specific energy but could also improve the stability of $Ti_3C_2T_x$-based supercapacitors.

Here, we have successfully intercalated RTIL cations—Em and Bm—into the 2D interlayers of $Ti_3C_2T_x$ via a simple chemical synthesis approach. The significantly enhanced interlayer space of $Ti_3C_2T_x$-Em and $Ti_3C_2T_x$-Bm was utilized for high-energy-storage supercapacitors. Firstly, $Ti_3C_2T_x$, $Ti_3C_2T_x$-Em, and $Ti_3C_2T_x$-Bm

Please cite this article in press as: Jadhav et al., Supercapacitive performance of ionic-liquid-intercalated two-dimensional $Ti_3C_2T_x$ in redox electrolyte, Cell Reports Physical Science (2024), https://doi.org/10.1016/j.xcrp.2024.101788

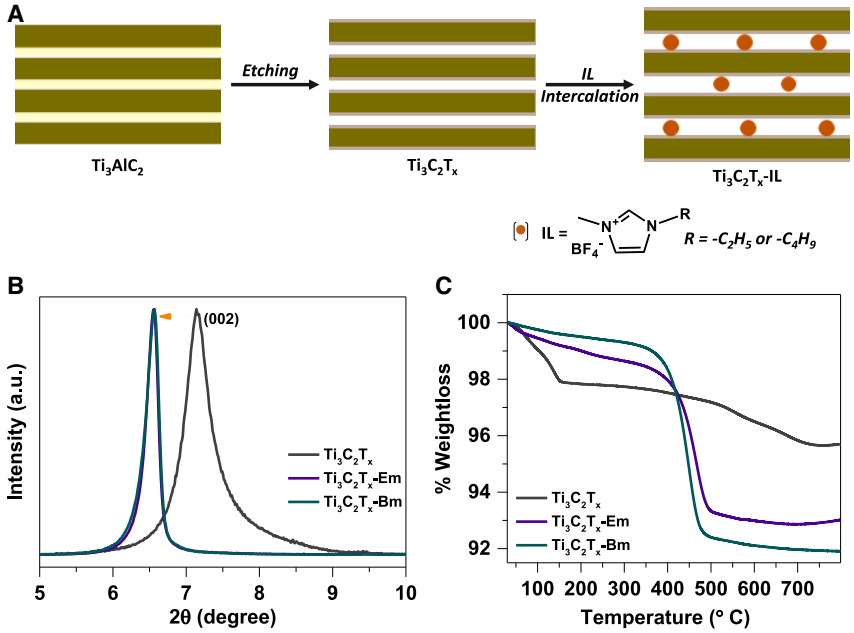

Figure 1. Intercalation of ionic liquids in $Ti_3C_2T_x$

(A) Schematic of the synthesis process of $Ti_3C_2T_x$ and $Ti_3C_2T_x$ -ionic liquid (IL).

(B and C) PXRD plots and TGA profiles of $Ti_3C_2T_x$, $Ti_3C_2T_x$-Em, and $Ti_3C_2T_x$-Bm.

symmetric supercapacitors were tested in an aqueous sulfuric acid electrolyte (potential window: 0–1 V), where inferior capacitance and poor cycling stability for all the materials were observed. To overcome this issue, we have used aqueous sulfuric acid-potassium iodide as an electrolyte. Our redox electrolyte dramatically enhanced the capacitance and stability of all three materials. The gravimetric capacitance ($C_{gr.}$) was in the order $Ti_3C_2T_x$-Em (725 F g^{-1}) > $Ti_3C_2T_x$-Bm (650 F g^{-1}) > $Ti_3C_2T_x$ (480 F g^{-1}), with 90% capacitance stability over 10,000 continuous charge-discharge cycles. Our concept of using an intercalant that not only enhances the interlayer space of $Ti_3C_2T_x$ but also interacts with the redox electrolyte will help boost the overall capacitance of the MXene materials.

RESULTS AND DISCUSSION

Synthesis and characterization of $Ti_3C_2T_x$ and ionic-liquid-intercalated $Ti_3C_2T_x$

We have synthesized $Ti_3C_2T_x$ from Ti_3AlC_2 following the modified etching process using LiF+HCl (experimental procedures; Figure S1).[39] Intercalation of IL was achieved simply by stirring $Ti_3C_2T_x$ in aqueous $EMIMBF_4$ ($EmBF_4$) or $BMIMBF_4$ ($BmBF_4$) solutions for 16 h (Figure 1A). $Ti_3C_2T_x$, $Ti_3C_2T_x$-Em, and $Ti_3C_2T_x$-Bm were characterized by powder X-ray diffraction (PXRD), thermogravimetric analysis (TGA), field-emission scanning electron microscopy (FESEM), and X-ray photoelectron spectroscopy (XPS) (Figures 1B, 1C, 2, and S2–S4).

The successful synthesis of $Ti_3C_2T_x$ from Ti_3AlC_2 was confirmed by observing a shift in the (002) PXRD peak toward a lower 2θ and by the absence of a peak at 38.4° (corresponding to aluminum) (Figure S1C). For the synthesis of $Ti_3C_2T_x$-Em and $Ti_3C_2T_x$-Bm, the reaction time was sufficient to facilitate Em and Bm intercalation in $Ti_3C_2T_x$ via the ion-exchange process (Li^+ deintercalation), leading to a downshift of the (002) PXRD peak (Figure 1B). Furthermore, the d spacing of $Ti_3C_2T_x$ increased from ~12.46 (2θ = 7.1°) to ~13.5 (2θ = 6.55°) and ~13.48 Å (2θ = 6.56°) for $Ti_3C_2T_x$-Em

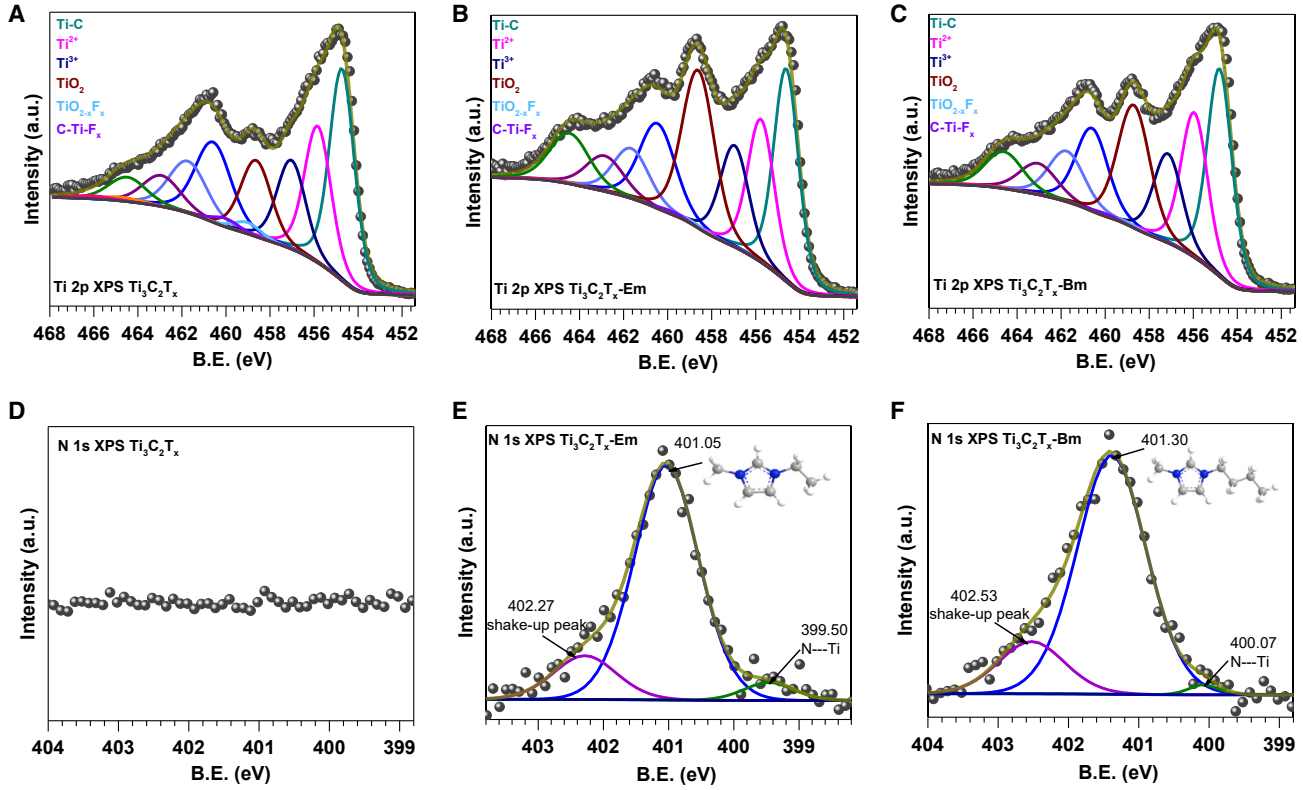

Figure 2. X-ray photoelectron spectroscopy (XPS) analysis of IL-intercalated $Ti_3C_2T_x$

(A–C) Ti 2p XPS spectra of $Ti_3C_2T_x$, $Ti_3C_2T_x$-Em, and $Ti_3C_2T_x$-Bm.

(D–F) N 1s XPS spectra of $Ti_3C_2T_x$, $Ti_3C_2T_x$-Em, and $Ti_3C_2T_x$-Bm.

and $Ti_3C_2T_x$-Bm, respectively, supporting the intercalation.[24] The IL-intercalated $Ti_3C_2T_x$ is more crystalline than parent $Ti_3C_2T_x$, as seen from the increased intensity and narrowed width of the (002) peak (Figures 1B and S2). Additionally, the non-basal peak at around 60° (2θ) confirms the maintenance of long-range order even after IL intercalation (Figure S2, inset).[28] Considering the size of Em and Bm (Figure S2), similar d spacings of $Ti_3C_2T_x$-Em and $Ti_3C_2T_x$-Bm, and the extent of increased interlayer space after the intercalation, the orientation of Em and Bm could be either parallel or tilted to the $Ti_3C_2T_x$ surface.[24] TGA of $Ti_3C_2T_x$, $Ti_3C_2T_x$-Em, $Ti_3C_2T_x$-Bm, $EmBF_4$, and $BmBF_4$ was performed to investigate the thermal stability of the materials and the loading of ILs (Figures 1C and S3). After heating $Ti_3C_2T_x$ to 800°C, only 4% weight loss is seen, attributed to the removal of a minute amount of water (~1%) and functional groups from the matrix. The onset decomposition temperature of pure $EmBF_4$ was slightly higher than for pure $BmBF_4$ (Figure S3), and a similar trend is observed in $Ti_3C_2T_x$-Em and $Ti_3C_2T_x$-Bm (Figures 1C and S3B). Moreover, the onset of the decomposition temperature of $Ti_3C_2T_x$-Em and $Ti_3C_2T_x$-Bm is higher (>80°C) than for pure ILs ($EmBF_4$ and $BmBF_4$), indicating a strong interaction between IL cations and the negatively charged $Ti_3C_2T_x$ framework (Figure S3B). After comparing the individual TGA curves of parent and composite materials, the loadings of Em and Bm are estimated to be ~5% and ~7% w/w in $Ti_3C_2T_x$-Em and $Ti_3C_2T_x$-Bm, respectively (Figure S3B). The initial weight loss in $Ti_3C_2T_x$-Em is due to the removal of water interacting with Em cations. $Ti_3C_2T_x$ has a fixed amount of negative charge on the surface due to the functional groups; therefore, it can only accommodate a certain amount of positive charge to maintain charge neutrality. Due to the higher positive inductive effect (+I effect) of the butyl (in Bm) compared

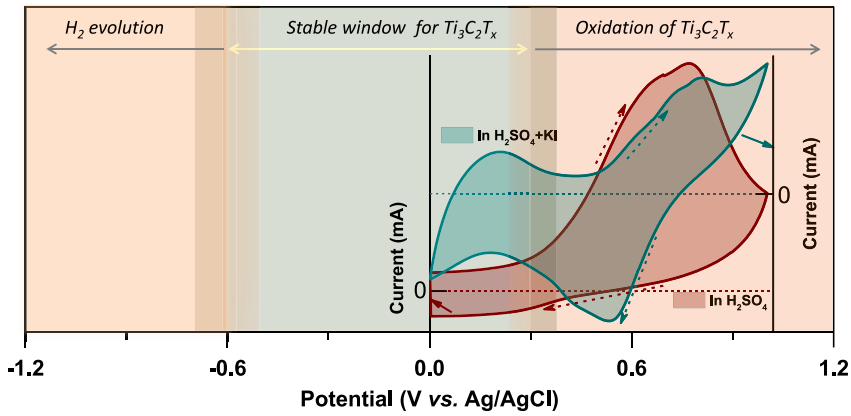

Figure 3. Stable potential window of $Ti_3C_2T_x$

Potential window showing stability region of $Ti_3C_2T_x$. Inset: CV plot recorded for the as-synthesized $Ti_3C_2T_x$ in 1 M H_2SO_4 and 1 M H_2SO_4+0.1 M KI in the three-electrode setup.

to the ethyl (in Em), a lower positive charge density is expected on Bm, resulting in its higher loading in $Ti_3C_2T_x$.[40] FESEM images showed layered morphology of $Ti_3C_2T_x$, $Ti_3C_2T_x$-Em, and $Ti_3C_2T_x$-Bm, suggesting the intact 2D backbone of $Ti_3C_2T_x$ after the intercalation of Em and Bm molecules, further corroborating the crystalline nature of PXRD (Figure S4). The electrical conductivities of $Ti_3C_2T_x$, $Ti_3C_2T_x$-Em, and $Ti_3C_2T_x$-Bm were calculated to be around 580, 110, and 113 S m^{-1}, respectively. A decrease in the conductivity value for IL-intercalated $Ti_3C_2T_x$ could be due to the presence of electrically insulating organic molecules inside the interlayers (Figure S5).

The XPS analysis confirmed (1) the successful synthesis of $Ti_3C_2T_x$ and (2) the presence of ILs in $Ti_3C_2T_x$-Em and $Ti_3C_2T_x$-Bm (Figure 2). The Ti 2p spectra of $Ti_3C_2T_x$, $Ti_3C_2T_x$-Em, and $Ti_3C_2T_x$-Bm were fitted with six doublets (Figures 2A–2C). The peaks centered at around 454.7, 455.8, and 457.1 eV correspond to Ti-C, Ti^{2+} ($Ti_3C_2(OH)_x$), and Ti^{3+} ($Ti_3C_2O_x$), respectively.[41] Peaks at around 458.7 and 459.1 eV are attributed to TiO_2 and $TiO_{2-x}F_x$, respectively.[41] The peak at around 460 eV is associated with C-Ti-F_x.[42] After the intercalation of ILs, a slight increment of the TiO_2 peak is due to the partial surface oxidation of $Ti_3C_2T_x$ by water molecules (Figures 1C and 2A–2C). However, due to the minute quantity, the PXRD signal of TiO_2 nanoparticles is completely absent in all three materials (Figure S2).[43] The N 1s XPS spectra of $Ti_3C_2T_x$-Em and $Ti_3C_2T_x$-Bm was deconvoluted into three peaks (Figures 2D–2F). The major peaks at binding energies of 401.05 and 401.30 eV for $Ti_3C_2T_x$-Em and $Ti_3C_2T_x$-Bm, respectively, were attributed to the two equivalent nitrogen atoms in the imidazolium ring, thus affirming the presence of Em and Bm in the respective $Ti_3C_2T_x$ interlayers.[44] In IL-intercalated materials, a noticeable shake-up peak at 402.27/402.53 eV appears, indicating the energy loss of the photoelectron.[45] Additional peaks at 399.50 and 400.07 eV for $Ti_3C_2T_x$-Em and $Ti_3C_2T_x$-Bm, respectively, assigned to the interaction between nitrogen and titanium, confirms the interactivity of ILs and the $Ti_3C_2T_x$.[46] $Ti_3C_2T_x$ does not contain any nitrogen.

Electrochemical performance of $Ti_3C_2T_x$ and ionic-liquid-intercalated $Ti_3C_2T_x$

$Ti_3C_2T_x$ is unstable in a potential window of 0–1 V in the aqueous H_2SO_4 electrolyte, where its irreversible oxidation can be seen in a cyclic voltammetry plot (Figure 3). This is in line with previous literature reports.[17] Interestingly, after introducing KI in the H_2SO_4 electrolyte, a reversible redox CV curve appeared (Figure 3; redox pairs are discussed below). Furthermore, the iodine redox pairs interact with $Ti_3C_2T_x$ and probably prevent it from undergoing an irreversible oxidation, thus improving its

CellPress OPEN ACCESS

Cell Reports Physical Science Article

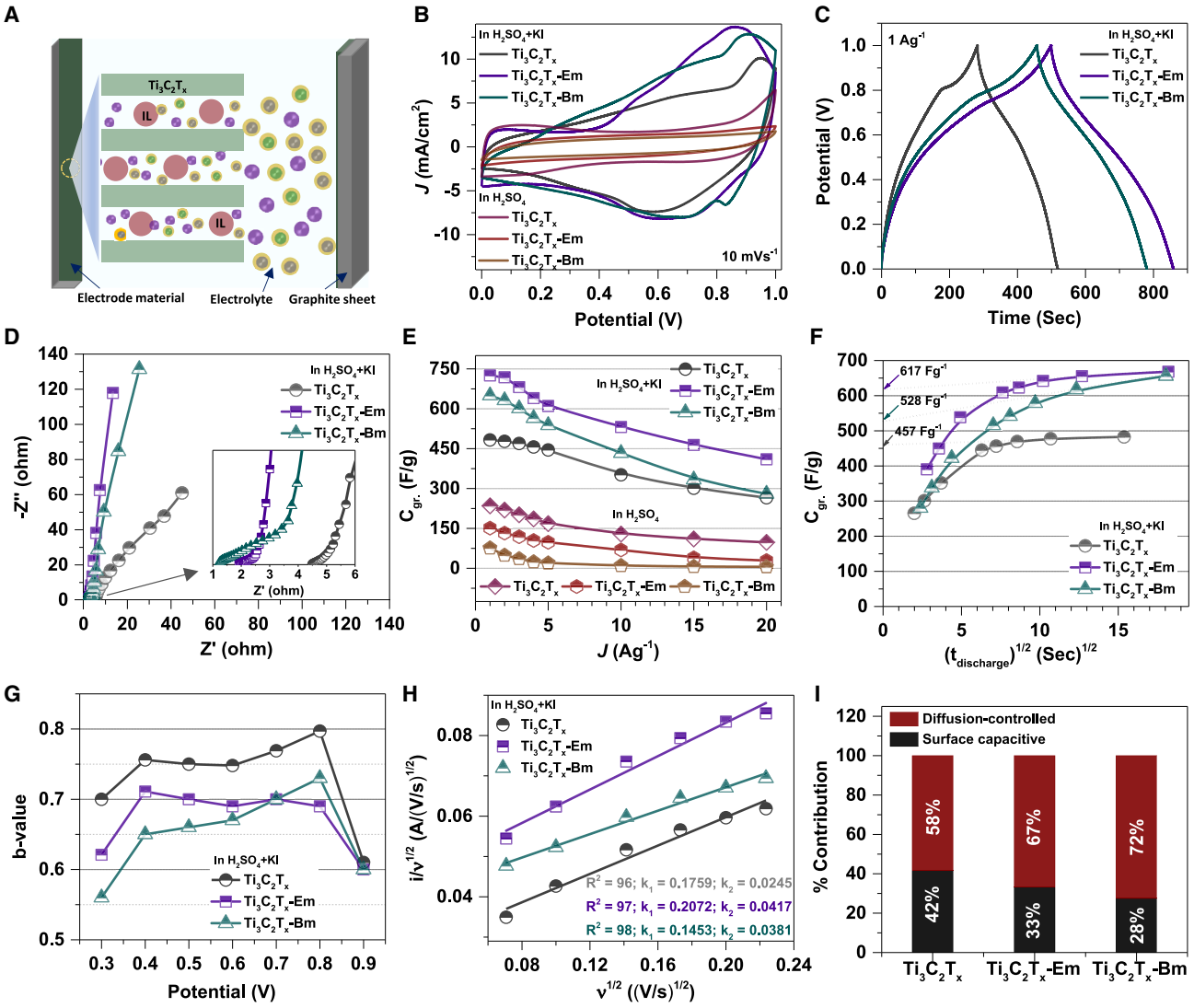

Figure 4. Electrochemical performance of $Ti_3C_2T_x$, $Ti_3C_2T_x$-Em, and $Ti_3C_2T_x$-Bm symmetric supercapacitors

(A) Schematic of symmetric two-electrode liquid-state supercapacitor setup and electrolyte percolation, including redox pair, into the electrode. Gray, cation; green, anion; purple, redox pair.

(B) CV plots of $Ti_3C_2T_x$, $Ti_3C_2T_x$-Em, and $Ti_3C_2T_x$-Bm in H_2SO_4 and H_2SO_4+KI electrolytes at a scan rate of 10 mV/s.

(C) GCD plots of $Ti_3C_2T_x$, $Ti_3C_2T_x$-Em, and $Ti_3C_2T_x$-Bm in H_2SO_4+KI electrolyte at a current density of 1 A/g.

(D) Nyquist plots of $Ti_3C_2T_x$, $Ti_3C_2T_x$-Em, and $Ti_3C_2T_x$-Bm in H_2SO_4+KI electrolyte. Inset: zoomed-in plot of high-frequency region.

(E) Gravimetric capacitances vs. current densities of $Ti_3C_2T_x$, $Ti_3C_2T_x$-Em, and $Ti_3C_2T_x$-Bm in H_2SO_4 and H_2SO_4+KI electrolytes.

(F) Rate-independent capacitances of $Ti_3C_2T_x$, $Ti_3C_2T_x$-Em, and $Ti_3C_2T_x$-Bm in H_2SO_4+KI electrolyte.

(G) *b*-values of $Ti_3C_2T_x$, $Ti_3C_2T_x$-Em, and $Ti_3C_2T_x$-Bm at different potentials (in H_2SO_4+KI electrolyte).

(H) k_1 and k_2 values of $Ti_3C_2T_x$, $Ti_3C_2T_x$-Em, and $Ti_3C_2T_x$-Bm in H_2SO_4+KI electrolyte (calculated using Equation 5).

(I) Percentage contribution of diffusion-controlled and surface capacitive processes of $Ti_3C_2T_x$, $Ti_3C_2T_x$-Em, and $Ti_3C_2T_x$-Bm at 0.5 V in H_2SO_4+KI electrolyte.

stability in higher-anodic-potential regions. This result implies that electrochemical stability of $Ti_3C_2T_x$-based materials in higher-anodic-potential regions can be achieved via the addition of an iodine redox pair to the H_2SO_4 electrolyte.

The supercapacitive performances of $Ti_3C_2T_x$, $Ti_3C_2T_x$-Em, and $Ti_3C_2T_x$-Bm were tested in symmetric two-electrode setups (Figures 4, 5, S6, S7, S10, and S12) using cyclic voltammetry (CV; scan rate [v] range 5–500 mV s^{-1}), galvanic charge-discharge

Cell Reports
Physical Science
Article

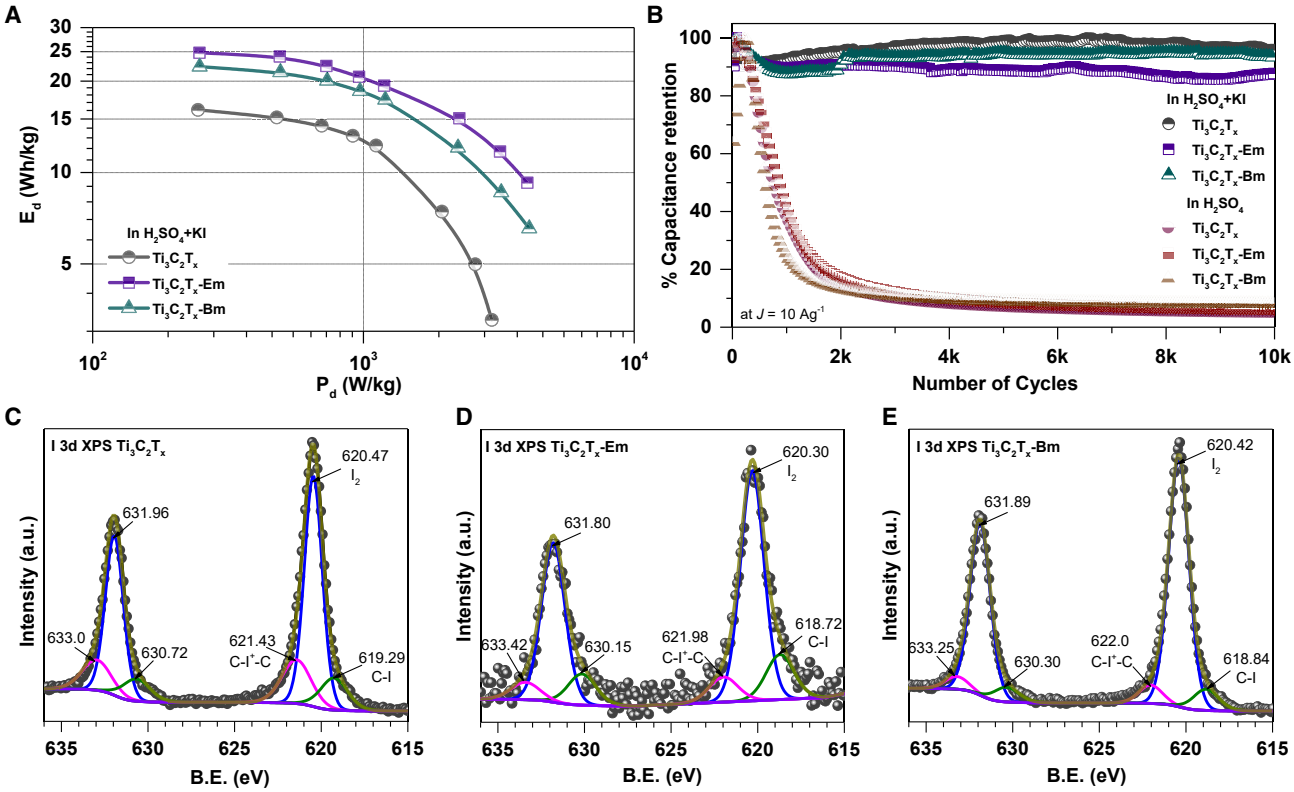

Figure 5. Cycling stability and XPS analysis of $Ti_3C_2T_x$, $Ti_3C_2T_x$-Em, and $Ti_3C_2T_x$-Bm

(A) Ragone plots of $Ti_3C_2T_x$, $Ti_3C_2T_x$-Em, and $Ti_3C_2T_x$-Bm in H_2SO_4+KI electrolyte.

(B) Cycling stability performance of $Ti_3C_2T_x$, $Ti_3C_2T_x$-Em, and $Ti_3C_2T_x$-Bm in H_2SO_4 and H_2SO_4+KI electrolytes.

(C–E) I 3d XPS plots of $Ti_3C_2T_x$, $Ti_3C_2T_x$-Em, and $Ti_3C_2T_x$-Bm after 10,000 GCD cycles in H_2SO_4+KI electrolyte.

(GCD; current density [J] range 1–20 Ag^{-1}), and electrochemical impedance spectroscopy (EIS; frequency range 1 MHz–1 mHz at 20 mV constant potential) techniques. In 1 M H_2SO_4 electrolyte solution and a potential window of 0–1 V, $Ti_3C_2T_x$, $Ti_3C_2T_x$-Em, and $Ti_3C_2T_x$-Bm showed partial rectangular CV and triangular GCD curves (Figures 4B and S6). The $C_{gr.}$ values of $Ti_3C_2T_x$, $Ti_3C_2T_x$-Em, and $Ti_3C_2T_x$-Bm were in the range of 76–234 F g^{-1} (Figure 4E). The higher capacitance of $Ti_3C_2T_x$ compared to IL-intercalated materials is probably due to the protons in aqueous acidic electrolyte having a higher chance of encountering the $Ti_3C_2T_x$ surface compared to $Ti_3C_2T_x$-Em and $Ti_3C_2T_x$-Bm, which have wider interlayer spacing. This promoted more surface redox activity inside the confined interlayer of $Ti_3C_2T_x$.[47] All three materials showed poor stability and degraded more than 80% within only 1,000 GCD cycles at a J of 10 A g^{-1} (Figure 5B). This is in line with previously reported literature where the $Ti_3C_2T_x$ backbone was found to be unstable in an aqueous acid electrolyte toward a higher anodic potential.[41] The gravimetric energy densities (E_d) of all three materials were below 10 Wh kg^{-1} (Figure S7).

In order to enhance the overall supercapacitive performances of $Ti_3C_2T_x$, $Ti_3C_2T_x$-Em, and $Ti_3C_2T_x$-Bm, we have used 1 M H_2SO_4+0.1 M KI (SA+KI) electrolyte solution. Iodide (I^-) is oxidized to iodine (I_2) by sulfuric acid (Equation 1). Since only 0.1 mol I^- per 1 mol H_2SO_4 is added, about 0.05 mol I_2 generation is expected. However, conversion of I^- to I_2 is slow in aqueous H_2SO_4 (Figure S8, inset), which gives enough time to form a dynamic equilibrium between triiodide (I_3^-) and I_2/I^- (Equation 2). UV-visible (UV-vis) absorption peaks at around 288 and 352 nm correspond to I_3^-,

whereas the peak at around 226 nm is due to I^- (Figure S8).[48] Under the applied potential, different iodine redox pairs ($3I^-/I_3^-$, $2I^-/I_2$, $2I_3^-/3I_2$, and $I_2/2IO_3$) could interact with the active electrode material and enhance the overall performance of the supercapacitor.[49] Notably, the conductivities of SA and SA+KI electrolytes are similar (Figure S8).

$$0.0625H_2SO_4 + 0.1KI \rightarrow 0.05K_2SO_4 + 0.05I_2 + 0.0125H_2S + 0.05H_2O \quad \text{(Equation 1)}$$

$$I_2 + I^- \leftrightarrow I_3^- \quad \text{(Equation 2)}$$

The initial CV scan at 50 mV s^{-1} for $Ti_3C_2T_x$, $Ti_3C_2T_x$-Em, and $Ti_3C_2T_x$-Bm shows a gradual rise in *J* and the emergence of redox peaks (Figure S9). These are attributed to the percolation of redox pairs into the interlayer space and their interaction with $Ti_3C_2T_x$. The *J* reaches saturation after several cycles, indicating the complete infiltration of electrolyte into the material. The subsequent electrochemical characterizations were performed after multiple CV scans at 50 mV s^{-1} (until the *J* saturated). Figure 4B shows the CV plots of $Ti_3C_2T_x$, $Ti_3C_2T_x$-Em, and $Ti_3C_2T_x$-Bm at a scan rate of 10 mV s^{-1}. All three materials exhibit redox peaks due to the interaction of iodine redox pairs from the electrolyte with the $Ti_3C_2T_x$. Notably, the $Ti_3C_2T_x$-Em composite shows a higher current response than $Ti_3C_2T_x$-Bm and $Ti_3C_2T_x$ in redox electrolyte. Redox activity in all three materials indicates that the charge storage is via the pseudocapacitance intercalation mechanism.[50] All three composites maintain good rate stability even at a very high scan rate of 500 mV s^{-1} (Figures S10A, S10D, and S10G). GCD measurement showed a non-rectangular curve of $Ti_3C_2T_x$, $Ti_3C_2T_x$-Em, and $Ti_3C_2T_x$-Bm, corroborating the CV (Figures 4C, S10B, S10E, and S10H). A longer discharge time is observed in the case of $Ti_3C_2T_x$-Em, followed by $Ti_3C_2T_x$-Bm and $Ti_3C_2T_x$, clearly demonstrating the better charge storage by Em-intercalated $Ti_3C_2T_x$ compared to Bm-intercalated and pristine $Ti_3C_2T_x$. The equivalent series resistance (R_s), charge-transfer resistance (R_{CT}), capacitive behavior, and time constant (τ_o) can be extracted from the EIS measurement.[51] From the Nyquist plot (Figure 4D), the R_s values of $Ti_3C_2T_x$-Em and $Ti_3C_2T_x$-Bm were found to be ~1.9 and ~1.2 Ω, respectively, which are lower than the R_s of $Ti_3C_2T_x$ (~4.5 Ω). The absence of complete semicircle formation at a high-frequency regime for all three materials implies a negligible R_{CT} at the electrode-electrolyte interface. Analysis of the low-frequency region suggested a better supercapacitive behavior of $Ti_3C_2T_x$-Em compared to $Ti_3C_2T_x$-Bm and $Ti_3C_2T_x$, where the Nyquist curve of the former appeared more parallel to the -Z″ axis than the latter. The faster charge-discharge rate of a capacitor can be extracted from the Bode phase plot.[52] The τ_o values ($\tau_o = 1/f_o$, where f_o is the frequency at a phase angle of −45°) of $Ti_3C_2T_x$, $Ti_3C_2T_x$-Em, and $Ti_3C_2T_x$-Bm were found to be around 4.9, 5.6, and 4.2 s, respectively (Figures S10C, S10F, and S10I). The $C_{gr.}$ of all the materials was calculated from GCD curves. Interestingly, the $C_{gr.}$ of $Ti_3C_2T_x$- Em was around 725 F g^{-1} at a *J* of 1 A g^{-1}, which is 1.5 times higher than for pristine $Ti_3C_2T_x$ and best among all reported $Ti_3C_2T_x$-based materials measured in an aqueous electrolyte by symmetric two-electrode setups (Figure 4E; Table S1). The $C_{gr.}$ of $Ti_3C_2T_x$-Bm was found to be around 650 F g^{-1} at a *J* of 1 A g^{-1}, which is slightly lower than $Ti_3C_2T_x$-Em but significantly higher than pristine $Ti_3C_2T_x$ (480 F g^{-1} at a *J* of 1 A g^{-1}) (Figure 4E). Though the interlayer distances in $Ti_3C_2T_x$-Em and $Ti_3C_2T_x$-Bm are similar, the extra degree of freedom of the larger alkyl chain and the slight hydrophobic nature of Bm could resist the hydrated ions during charging. In the two-electrode setup and redox electrolyte, the bare graphite sheet showed non-redox CV curves and low charge storage (Figure S11A). This further supports the direct involvement of $Ti_3C_2T_x$ and $Ti_3C_2T_x$- IL in redox activity. The rate-independent capacitance can be extracted from the following equation:

$$C = k_1 + k_2 v^{1/2} \quad \text{(Equation 3)}$$

where C is capacitance, k_1 is the rate-independent surface-controlled component, k_2 is the rate-dependent semi-infinite linear-diffusion-controlled component, and v is the discharge time.[52] Noticeably, the rate-independent capacitance of $Ti_3C_2T_x$-Em (617 F g^{-1}) was significantly higher than for $Ti_3C_2T_x$-Bm (528 F g^{-1}) and $Ti_3C_2T_x$ (458 F g^{-1}) (Figure 4F). Charge storage in supercapacitors is dominated by either a diffusion-controlled or surface capacitive process. Here, diffusion-controlled and surface capacitive processes at 0.3, 0.4, 0.5, 0.6, 0.7, 0.8, and 0.9 V were analyzed using the following equation[53]:

$$i(v) = av^b \quad \text{(Equation 4)}$$

where i is the current (in A), ν is the scan rate (in V/s) (ν = 0.005–0.05 V/s), and a and b are variables (Figures 4G and S13). The b-values for each material are between 0.55 and 0.8 (Figure 4G), which is known as the "transition" area between diffusion-controlled (b = 0.5) and surface capacitive (b = 1) processes.[54] Furthermore, since the clear boundary of both processes is difficult to define, b-values closer to 0.5 are considered as diffusion controlled and near 1 as surface capacitive. Notably, the charge storage in $Ti_3C_2T_x$-Em and $Ti_3C_2T_x$-Bm occurred mostly via the diffusion-controlled process (Figure 4G), which may be due to the higher interlayer spacing and iodine-pair adsorption. On the other hand, both the diffusion-controlled and surface capacitive processes were observed in the case of $Ti_3C_2T_x$ (Figure 4G). Moreover, the percentage contributions of both diffusion-controlled ($i_{diff-cont}$) and surface capacitive ($i_{surf-cap}$) processes were calculated by rearranging Equation 3, i.e.,[53]

$$i(V) = k_1 v + k_2 v^{1/2} = i_{surf-cap} + i_{diff-cont} \quad \text{(Equation 5)}$$

(Figures 4H and 4I, and details are given in the supplemental information; Figures S14–S17). The constants k_1 and k_2 were calculated at different potentials (0.3–0.9 V). Figure 4H displays k_1 and k_2 values determined at 0.5 V potential, which were subsequently used in Equation 5 to calculate $i_{diff-cont}$ and $i_{surf-cap}$. At a scan rate of 10 mV s^{-1} and 0.5 V potential, $Ti_3C_2T_x$ exhibited a 58% diffusion-controlled process compared to 67% and 72% for $Ti_3C_2T_x$-Em and $Ti_3C_2T_x$-Bm, respectively (Figure 4I). It is clear that after IL intercalation, the total capacitance is dominated by a Faradaic process, further supporting the pseudocapacitance intercalation mechanism.

The gravimetric energy density (E_d) and power density (P_d) values of $Ti_3C_2T_x$, $Ti_3C_2T_x$-Em, and $Ti_3C_2T_x$-Bm were calculated from GCD curves. $Ti_3C_2T_x$-Em showed remarkably high E_d and P_d of 24.8 Wh kg^{-1} (maximum E_d) and 4,031 W kg^{-1} (maximum P_d), respectively, which are slightly higher than those for $Ti_3C_2T_x$-Bm (max. E_d = 22.3 Wh kg^{-1} and similar max. P_d = 4,100 W kg^{-1}); however, they are ~1.5 times higher than pristine $Ti_3C_2T_x$ (max. E_d = 16.1 Wh kg^{-1} and max. P_d = 2,980 W kg^{-1}) (Figure 5A). Such superior E_d and P_d values of $Ti_3C_2T_x$-Em and $Ti_3C_2T_x$-Bm provide encouraging evidence for the inclusion of small redox molecules in an aqueous acidic electrolyte for intercalated MXene-based systems. The practical application of a supercapacitor can only be realized if it can sustain multiple charge-discharge cycles. The electrodes of $Ti_3C_2T_x$, $Ti_3C_2T_x$-Em, and $Ti_3C_2T_x$-Bm were subjected to 10,000 continuous GCD cycles at a J of 10 A g^{-1} (Figure 5B). Surprisingly, around 90% capacitance retention was observed for all three materials, unlike cycling in only the H_2SO_4 electrolyte, where electrode materials severely degraded well before 1,000 GCD cycles (Figure 5B). The coulombic efficiencies of all the electrodes were ~100%, which indicates the facile charge percolation inside

the 2D interlayers of the electrodes throughout the continuous GCD cycles (Figure S12). After the completion of electrochemical characterization and 10,000 GCD cycles, the morphologies of the materials remained intact, as can be seen from the SEM images (Figure S18).

From electrochemical characterization, it was clear that the use of the optimal amount of KI in the H_2SO_4 solution not only enhanced the capacitance values but also inhibited the material deterioration even after 10,000 continuous charge-discharge cycles. Furthermore, we have recorded I 3d XPS of electrodes after 10,000 cycles (Figures 5C–5E). Two doublets, I $3d_{5/2}$ and I $3d_{3/2,}$ centered at around 620.4 and 631.8 eV, respectively, were deconvoluted into six peaks.[55,56] For all three materials ($Ti_3C_2T_x$/$Ti_3C_2T_x$-Em/$Ti_3C_2T_x$-Bm), the major I $3d_{5/2}$ peak at 620.47/620.30/620.42 eV is assigned to the iodine molecule, whereas peaks at 619.29/618.72/618.84 and 621.43/621.98/622.0 eV were assigned to C–I and C–I^+–C bonding, respectively (Figures 5C–5E). The presence of iodine in different oxidation states in all three electrode materials corroborates with CV plots and emphasizes the pseudocapacitance intercalation mechanism. The binding energies (B.E.) of I_2 for all three electrode materials were similar; however, we observed a significant shift of C-I and C-I^+-C peaks with respect to the I_2 peak in $Ti_3C_2T_x$-Em and $Ti_3C_2T_x$-Bm compared to $Ti_3C_2T_x$, suggesting the strong interaction of iodine with the IL-intercalated $Ti_3C_2T_x$ (Figures 5C–5E). The presence of nitrogen in the interlayers of $Ti_3C_2T_x$ increases the adsorption energy of the materials, which in turn enhances the stability of the iodine adsorbed. Furthermore, sufficient amount of iodine inside the interlayer space increases the number of redox reactions between redox pairs and the $Ti_3C_2T_x$ framework.[55,56] Overall, the enhanced electrochemical performances of $Ti_3C_2T_x$-Em and $Ti_3C_2T_x$-Bm are credited to Em and Bm for (1) increasing the interlayer space of 2D layered $Ti_3C_2T_x$, (2) interacting with the $Ti_3C_2T_x$ framework, and (3) increasing the high iodine loading.

In conclusion, we report the successful intercalation of two types of RTILs ($EmBF_4$~5% w/w and $BmBF_4$~7% w/w) into the interlayers of 2D-$Ti_3C_2T_x$. The fabricated electrodes of $Ti_3C_2T_x$, $Ti_3C_2T_x$-Em, and $Ti_3C_2T_x$-Bm were tested for supercapacitor applications in a symmetric two-electrode setup in a potential window of 0–1 V. Electrochemical measurements in 1 M H_2SO_4 electrolyte in the same potential window showed both poor capacitance and charge-discharge cycle stability due to the instability of materials in anodic potentials. To address this issue, we employed a combination of sulfuric acid and potassium iodide as an electrolyte and elevated the overall performance of $Ti_3C_2T_x$, $Ti_3C_2T_x$-Em, and $Ti_3C_2T_x$-Bm supercapacitors. The $C_{gr.}$ values of $Ti_3C_2T_x$, $Ti_3C_2T_x$-Em and $Ti_3C_2T_x$-Bm were found to be around 480, 725, and 650 Fg^{-1}, respectively. These values are remarkably high and represent the best performance among $Ti_3C_2T_x$-based materials tested in similar electrode setups. Interestingly, the capacitance values increased by approximately 1.5 times compared to pristine $Ti_3C_2T_x$ after the intercalation of ILs, in the redox electrolytic system. All the materials showed very high stability of around 90% capacitance retention after 10,000 continuous GCD cycles. We propose two major reasons behind the enhanced supercapacitive performances of $Ti_3C_2T_x$-Em and $Ti_3C_2T_x$-Bm. Firstly, the intercalation of ILs resulted in an expanded interlayer space between the 2D sheets of $Ti_3C_2T_x$, allowing for a higher number of charges to be accommodated and facilitating the percolation of electrolytic ions. Secondly, in the presence of the H_2SO_4+KI electrolyte, *in-situ*-generated iodine exhibited its characteristic redox behavior, entering the interlayers of $Ti_3C_2T_x$-Em and $Ti_3C_2T_x$-Bm electrodes and interacting with the $Ti_3C_2T_x$ and IL backbones. These combined effects contributed to the significant enhancement in supercapacitive performance. Our work

demonstrates how small redox molecules (with anodic reduction potential) in aqueous acidic electrolytes can improve the supercapacitive performance of MXene-intercalant systems. This method can be applied to other similar systems for enhanced energy storage. Our synthesized $Ti_3C_2T_x$-Em and $Ti_3C_2T_x$-Bm could be promising candidates for Li-I_2 batteries.

EXPERIMENTAL PROCEDURES

Resource availability

Lead contact

Further information and requests for resources should be directed to and will be fulfilled by the lead contact, Carita Kvarnström (carkva@utu.fi).

Materials availability

This study did not generate unique reagents.

Data and code availability

The data that support the findings of this study are available from the lead contact upon reasonable request.

Materials

Ti_3AlC_2 (MAX) was purchased from y-Carbon (Kiev, Ukraine). LiF (98.5%) was purchased from Alfa Aesar. Hydrochloric acid (HCl; 37%) was purchased from VWR Chemicals. The ILs $EMIMBF_4$ (99%) and $BMIMBF_4$ (99%) were purchased from Iolitec (Heilbronn, Germany). Sulfuric acid (H_2SO_4; 1 M) and potassium iodide (KI) were purchased from Merck. A 5% Nafion solution in water and alcohol was purchased from Aldrich. 1-Methyl-2-pyrrolidone (NMP; >99% purity) was purchased from TCI Chemicals. TIMCAL super P conducting carbon black was bought from Nanografi Nano Technology, and graphite sheet (99.88% purity, 0.25 mm thickness) was purchased from Thermo Scientific. All materials were used as received unless mentioned otherwise.

Synthesis of $T_3C_2T_x$

$Ti_3C_2T_x$ was synthesized using the MILD method. Briefly, in a PTFE bottle, 750 mg LiF was added to 15 mL (6 M) HCl solution. The mixture was stirred at RT until all the LiF was dissolved. To this, 750 mg Ti_3AlC_2 was added in portions over 5 min to avoid the initial overheating. Once all the Ti_3AlC_2 was added, the bottles were loosely capped and immersed in an oil bath preheated at 45°C under constant stirring for 48 h. The reaction was cooled to RT, and the obtained product was transferred to a 50 mL centrifuge tube prefilled with 20 mL quartz double-distilled (DD) water and centrifuged several times at 3,500 rpm for 5 min. The procedure was repeated until the pH of the supernatant became >5. Lastly, the obtained $Ti_3C_2T_x$ was re-dispersed in a small amount of DD water and was vacuum filtered over a cellulose nitrate paper, followed by drying in a vacuum desiccator for 24 h.

Synthesis of $Ti_3C_2T_x$-Em and $TI_3C_2T_x$-Bm

2 mL of $EMIMBF_4$ ($EmBF_4$) and $BMIMBF_4$ ($BmBF_4$) were stirred separately in 40 mL DD H_2O for 5 min at RT to ensure their complete solubility. 130 mg layered $Ti_3C_2T_x$ was added to the solution and sonicated for 15 min, followed by de-aerating with Ar gas for 30 min. The reaction bottles were covered with aluminum foil and stirred for 16 h at RT. After 16 h, the products were washed with water (15 mL, 5 times) and ethanol (2 mL, 5 times) via centrifugation at 3,500 rpm for 5 min, followed by drying in a vacuum desiccator at RT for 24 h.

Characterization

PXRD was performed on PANalytical Aeris with Cu Kα radiation (Kα = 1.564 Å). TGA (under N_2 atmosphere) was performed using TA Instruments Q600 SDT. The morphology of the materials was analyzed using Thermo Scientific Apreo S FESEM. Four probe current-voltage (I-V) measurements on pressed pellets (5 tons) were recorded using a Keithley 2460 source meter. UV-vis data were collected using a Cary 60 spectrophotometer (Agilent). XPS measurements were performed using Thermo Scientific Nexsa XPS with a monochromatized Al Kα (1,486.7 eV) source under a base vacuum of $\sim 10^{-9}$ mbar. The pass energy of 50 eV was used to collect the core-level spectra. The spot size was 200 μm, and dual-charge compensation was applied. Ti 2p XPS and N 1s XPS spectra were fitted with Voigt line shape, and the effect of inelastically scattered photoelectrons was removed using Shirley and Avantage Smart (I 3d) background subtraction methods. All the electrochemical measurements were done using Iviumstat (IVIUM) and a BioLogic SP-150e galvanostat/potentiostat workstation.

Preparation of electrodes

The ink for active electrodes was made by mixing 90 wt % active material, 5 wt % conducting carbon, and 5 wt % Nafion solution in NMP solvent. The ink was then coated on a conducting graphite sheet such that the loading of the material was 2 mg/cm^2. The electrodes were dried in an oven at 100°C for 7 h. The three-electrode test of the $Ti_3C_2T_x$ electrode was performed in 1 M H_2SO_4 and 1 M H_2SO_4+0.1 M KI electrolytes, where graphite rod and silver wire coated with AgCl were used as counter- and quasi-reference electrodes (Ag/AgCl against Fe^{2+}/Fe^{3+}; Figure S11B) respectively. Supercapacitor testing was performed in symmetric two-electrode setups both in 1 M H_2SO_4 and 1 M H_2SO_4+0.1 M KI electrolytes.

SUPPLEMENTAL INFORMATION

Supplemental information can be found online at https://doi.org/10.1016/j.xcrp.2024.101788.

ACKNOWLEDGMENTS

A.J. and P.K.J. acknowledge the Real Estate Foundation, Finland, and Business Finland (COMPOL project) for their financial support. A.J. and P.K.J. thank Dr. Pekka Peljo and Gabriel Gonzalez for providing access to the BioLogic SP-150e.

AUTHOR CONTRIBUTIONS

A.J. planned the experimental sessions and performed most of the experiments. A.J. and P.K.J. performed electrochemical measurements. S.G., M.S., and P.D. helped with the characterizations. A.J. and P.K.J. wrote the manuscript with supervision and input from C.K.

DECLARATION OF INTERESTS

The authors declare no competing interests.

Received: June 20, 2023
Revised: November 22, 2023
Accepted: January 5, 2024
Published: January 30, 2024

REFERENCES

1. Chu, S., and Majumdar, A. (2012). Opportunities and challenges for a sustainable energy future. Nature *488*, 294–303.
2. Sutherland, B.R. (2019). Charging up Stationary Energy Storage. Joule *3*, 1–3.
3. Winter, M., and Brodd, R.J. (2004). What are batteries, fuel cells, and supercapacitors? Chem. Rev. *104*, 4245–4269.
4. Simon, P., Gogotsi, Y., and Dunn, B. (2014). Where do batteries end and supercapacitors begin? Science *343*, 1210–1211.
5. Conway, B.E. (2013). Electrochemical Supercapacitors: Scientific Fundamentals and Technological Applications (Springer Science & Business Media).
6. Lukatskaya, M.R., Dunn, B., and Gogotsi, Y. (2016). Multidimensional materials and device architectures for future hybrid energy storage. Nat. Commun. *7*, 12647.
7. Simon, P., and Gogotsi, Y. (2008). Materials for electrochemical capacitors. Nat. Mater. *7*, 845–854.
8. Nakhanivej, P., Yu, X., Park, S.K., Kim, S., Hong, J.-Y., Kim, H.J., Lee, W., Hwang, J.Y., Yang, J.E., Wolverton, C., et al. (2019). Revealing molecular-level surface redox sites of controllably oxidized black phosphorus nanosheets. Nat. Mater. *18*, 156–162.
9. Anasori, B., Lukatskaya, M.R., and Gogotsi, Y. (2017). 2D metal carbides and nitrides (MXenes) for energy storage. Nat. Rev. Mater. *2*, 16098.
10. Hu, M., Zhang, H., Hu, T., Fan, B., Wang, X., and Li, Z. (2020). Emerging 2D MXenes for supercapacitors: status, challenges and prospects. Chem. Soc. Rev. *49*, 6666–6693.
11. Naguib, M., Kurtoglu, M., Presser, V., Lu, J., Niu, J., Heon, M., Hultman, L., Gogotsi, Y., and Barsoum, M.W. (2011). Two-dimensional nanocrystals produced by exfoliation of Ti_3AlC_2. Adv. Mater. *23*, 4248–4253.
12. Naguib, M., Mashtalir, O., Carle, J., Presser, V., Lu, J., Hultman, L., Gogotsi, Y., and Barsoum, M.W. (2012). Two-dimensional transition metal carbides. ACS Nano *6*, 1322–1331.
13. Okubo, M., Sugahara, A., Kajiyama, S., and Yamada, A. (2018). MXene as a charge storage host. Acc. Chem. Res. *51*, 591–599.
14. Li, X., Huang, Z., Shuck, C.E., Liang, G., Gogotsi, Y., and Zhi, C. (2022). MXene chemistry, electrochemistry and energy storage applications. Nat. Rev. Chem *6*, 389–404.
15. Gund, G.S., Park, J.H., Harpalsinh, R., Kota, M., Shin, J.H., Kim, T.-i., Gogotsi, Y., and Park, H.S. (2019). MXene/Polymer Hybrid Materials for Flexible AC-Filtering Electrochemical Capacitors. Joule *3*, 164–176.
16. Zhao, M.Q., Trainor, N., Ren, C.E., Torelli, M., Anasori, B., and Gogotsi, Y. (2019). Scalable manufacturing of large and flexible sheets of MXene/graphene heterostructures. Adv. Mater. Technol. *4*, 1800639.
17. Zhao, M.Q., Ren, C.E., Ling, Z., Lukatskaya, M.R., Zhang, C., Van Aken, K.L., Barsoum, M.W., and Gogotsi, Y. (2015). Flexible MXene/carbon nanotube composite paper with high volumetric capacitance. Adv. Mater. *27*, 339–345.
18. Chen, H., Ma, H., and Li, C. (2021). Host–guest intercalation chemistry in MXenes and its implications for practical applications. ACS Nano *15*, 15502–15537.
19. Luo, J., Zhang, W., Yuan, H., Jin, C., Zhang, L., Huang, H., Liang, C., Xia, Y., Zhang, J., Gan, Y., and Tao, X. (2017). Pillared structure design of MXene with ultralarge interlayer spacing for high-performance lithium-ion capacitors. ACS Nano *11*, 2459–2469.
20. Lukatskaya, M.R., Mashtalir, O., Ren, C.E., Dall'Agnese, Y., Rozier, P., Taberna, P.L., Naguib, M., Simon, P., Barsoum, M.W., and Gogotsi, Y. (2013). Cation intercalation and high volumetric capacitance of two-dimensional titanium carbide. Science *341*, 1502–1505.
21. Liu, W., Li, L., Hu, C., Chen, D., and Shen, G. (2022). Intercalation of Small Organic Molecules into $Ti_3C_2T_x$ MXene Cathodes for Flexible High-Volume-Capacitance Zn-Ion Microsupercapacitor. Adv. Mater. Technol. *7*, 2200158.
22. Mashtalir, O., Naguib, M., Mochalin, V.N., Dall'Agnese, Y., Heon, M., Barsoum, M.W., and Gogotsi, Y. (2013). Intercalation and delamination of layered carbides and carbonitrides. Nat. Commun. *4*, 1716.
23. Liang, K., Matsumoto, R.A., Zhao, W., Osti, N.C., Popov, I., Thapaliya, B.P., Fleischmann, S., Misra, S., Prenger, K., Tyagi, M., et al. (2021). Engineering the Interlayer Spacing by Pre-Intercalation for High Performance Supercapacitor MXene Electrodes in Room Temperature Ionic Liquid. Adv. Funct. Mater. *31*, 2104007.
24. Jäckel, N., Krüner, B., Van Aken, K.L., Alhabeb, M., Anasori, B., Kaasik, F., Gogotsi, Y., and Presser, V. (2016). Electrochemical in situ tracking of volumetric changes in two-dimensional metal carbides (MXenes) in ionic liquids. ACS Appl. Mater. Interfaces *8*, 32089–32093.
25. Zheng, S., Zhang, C.J., Zhou, F., Dong, Y., Shi, X., Nicolosi, V., Wu, Z.-S., and Bao, X. (2019). Ionic liquid pre-intercalated MXene films for ionogel-based flexible micro-supercapacitors with high volumetric energy density. J. Mater. Chem. A *7*, 9478–9485.
26. Armand, M., Endres, F., MacFarlane, D.R., Ohno, H., and Scrosati, B. (2009). Ionic-liquid materials for the electrochemical challenges of the future. Nat. Mater. *8*, 621–629.
27. Lian, C., Liu, H., Li, C., and Wu, J. (2019). Hunting ionic liquids with large electrochemical potential windows. AIChE J. *65*, 804–810.
28. Yan, F., Zhang, C., Wang, H., Zhang, X., Zhang, H., Jia, H., Zhao, Y., and Wang, J. (2021). A coupled conductor of ionic liquid with Ti_3C_2 MXene to improve electrochemical properties. J. Mater. Chem. A *9*, 442–452.
29. Zhong, C., Deng, Y., Hu, W., Qiao, J., Zhang, L., and Zhang, J. (2015). A review of electrolyte materials and compositions for electrochemical supercapacitors. Chem. Soc. Rev. *44*, 7484–7539.
30. Borenstein, A., Strauss, V., Kowal, M.D., Yoonessi, M., Muni, M., Anderson, M., and Kaner, R.B. (2018). Laser-reduced graphene-oxide/ferrocene: a 3-D redox-active composite for supercapacitor electrodes. J. Mater. Chem. A *6*, 20463–20472.
31. Ma, R., Cao, L., Zhuo, J., Lu, J., Chen, J., Huang, J., Yang, G., and Yi, F. (2023). Designed Redox-Electrolyte Strategy Boosted with Electrode Engineering for High-Performance $Ti_3C_2T_x$ MXene-Based Supercapacitors. Adv. Energy Mater. *13*, 2301219.
32. Hwang, J.Y., El-Kady, M.F., Li, M., Lin, C.-W., Kowal, M., Han, X., and Kaner, R.B. (2017). Boosting the capacitance and voltage of aqueous supercapacitors via redox charge contribution from both electrode and electrolyte. Nano Today *15*, 15–25.
33. Chen, Y.-C., and Lin, L.-Y. (2019). Investigating the redox behavior of activated carbon supercapacitors with hydroquinone and p-phenylenediamine dual redox additives in the electrolyte. J. Colloid Interface Sci. *537*, 295–305.
34. Vonlanthen, D., Lazarev, P., See, K.A., Wudl, F., and Heeger, A.J. (2014). A Stable Polyaniline-Benzoquinone-Hydroquinone Supercapacitor. Adv. Mater. *26*, 5095–5100.
35. Hashemi, M., Rahmanifar, M.S., El-Kady, M.F., Noori, A., Mousavi, M.F., and Kaner, R.B. (2018). The use of an electrocatalytic redox electrolyte for pushing the energy density boundary of a flexible polyaniline electrode to a new limit. Nano Energy *44*, 489–498.
36. Shabangoli, Y., Rahmanifar, M.S., El-Kady, M.F., Noori, A., Mousavi, M.F., and Kaner, R.B. (2018). Thionine Functionalized 3D Graphene Aerogel: Combining Simplicity and Efficiency in Fabrication of a Metal-Free Redox Supercapacitor. Adv. Energy Mater. *8*, 1802869.
37. Chun, S.-E., Evanko, B., Wang, X., Vonlanthen, D., Ji, X., Stucky, G.D., and Boettcher, S.W. (2015). Design of aqueous redox-enhanced electrochemical capacitors with high specific energies and slow self-discharge. Nat. Commun. *6*, 7818.
38. Kushwaha, R., Haldar, S., Shekhar, P., Krishnan, A., Saha, J., Hui, P., Vinod, C.P., Subramaniam, C., and Vaidhyanathan, R. (2021). Exceptional Capacitance Enhancement of a Non-Conducting COF through Potential-Driven Chemical Modulation by Redox Electrolyte. Adv. Energy Mater. *11*, 2003626.
39. Lipatov, A., Alhabeb, M., Lukatskaya, M.R., Boson, A., Gogotsi, Y., and Sinitskii, A. (2016). Effect of synthesis on quality, electronic properties and environmental stability of individual monolayer Ti_3C_2 MXene flakes. Adv. Electron. Mater. *2*, 1600255.
40. Zhao, H., Zhang, H., Wang, Z., Jiang, X., Xie, Y., Xu, Z., Wang, Y., and Yang, W. (2021). Chain-Elongated Ionic Liquid Electrolytes for Low

Self-Discharge All-Solid-State Supercapacitors at High Temperature. ChemSusChem *14*, 3895–3903.

41. Tang, J., Mathis, T.S., Kurra, N., Sarycheva, A., Xiao, X., Hedhili, M.N., Jiang, Q., Alshareef, H.N., Xu, B., Pan, F., and Gogotsi, Y. (2019). Tuning the electrochemical performance of titanium carbide MXene by controllable in situ anodic oxidation. Angew. Chemie. *58*, 17849–17855.

42. Natu, V., Benchakar, M., Canaff, C., Habrioux, A., Célérier, S., and Barsoum, M.W. (2021). A critical analysis of the X-ray photoelectron spectra of $Ti_3C_2T_z$ MXenes. Matter *4*, 1224–1251.

43. Cao, F., Zhang, Y., Wang, H., Khan, K., Tareen, A.K., Qian, W., Zhang, H., and Ågren, H. (2022). Recent advances in oxidation stable chemistry of 2D MXenes. Adv. Mater. *34*, 2107554.

44. Caporali, S., Bardi, U., and Lavacchi, A. (2006). X-ray photoelectron spectroscopy and low energy ion scattering studies on 1-buthyl-3-methyl-imidazolium bis (trifluoromethane) sulfonimide. J. Electron Spectros. Relat. Phenomena *151*, 4–8.

45. Capitán, M.J., Álvarez, J., and Navio, C. (2018). Study of the electronic structure of electron accepting cyano-films: TCNQ versus TCNE. Phys. Chem. Chem. Phys. *20*, 10450–10459.

46. Kochrekar, S., Kalekar, A., Mehta, S., Damlin, P., Salomäki, M., Granroth, S., Meltola, N., Joshi, K., and Kvarnström, C. (2021). Copolymers of bipyridinium and metal (Zn & Ni) porphyrin derivatives; theoretical insights and electrochemical activity towards CO_2. RSC Adv. *11*, 19844–19855.

47. Sun, Y., Zhan, C., Kent, P.R.C., Naguib, M., Gogotsi, Y., and Jiang, D.-e. (2020). Proton redox and transport in MXene-confined water. ACS Appl. Mater. Interfaces *12*, 763–770.

48. Skunik-Nuckowska, M., Lubera, J., Rączka, P., Mroziewicz, A.A., Dyjak, S., and Kulesza, P.J. (2022). Conducting Polymer-Based Hybrid Electrochemical Capacitor Utilizing Potassium Iodide Redox Electrolyte with Controlled Self-Discharge. Chemelectrochem *9*, e202101222.

49. Sun, Q., Li, Y., and He, T. (2019). The excellent capacitive capability for N, P-doped carbon microsphere/reduced graphene oxide nanocomposites in H_2SO_4/KI redox electrolyte. J. Mater. Sci. *54*, 7665–7678.

50. Mu, X., Wang, D., Du, F., Chen, G., Wang, C., Wei, Y., Gogotsi, Y., Gao, Y., and Dall'Agnese, Y. (2019). Revealing the pseudo-intercalation charge storage mechanism of MXenes in acidic electrolyte. Adv. Funct. Mater. *29*, 1902953.

51. Mei, B.-A., Munteshari, O., Lau, J., Dunn, B., and Pilon, L. (2018). Physical interpretations of Nyquist plots for EDLC electrodes and devices. J. Phys. Chem. C *122*, 194–206.

52. Jha, P.K., Gupta, K., Debnath, A.K., Rana, S., Sharma, R., and Ballav, N. (2019). 3D mesoporous reduced graphene oxide with remarkable supercapacitive performance. Carbon *148*, 354–360.

53. Wang, J., Polleux, J., Lim, J., and Dunn, B. (2007). Pseudocapacitive contributions to electrochemical energy storage in TiO_2 (anatase) nanoparticles. J. Phys. Chem. C *111*, 14925–14931.

54. Liu, J., Wang, J., Xu, C., Jiang, H., Li, C., Zhang, L., Lin, J., and Shen, Z.X. (2018). Advanced energy storage devices: basic principles, analytical methods, and rational materials design. Adv. Sci. *5*, 1700322.

55. Lu, K., Hu, Z., Ma, J., Ma, H., Dai, L., and Zhang, J. (2017). A rechargeable iodine-carbon battery that exploits ion intercalation and iodine redox chemistry. Nat. Commun. *8*, 527.

56. Zhang, G., Zhang, M., Ye, X., Qiu, X., Lin, S., and Wang, X. (2014). Iodine modified carbon nitride semiconductors as visible light photocatalysts for hydrogen evolution. Adv. Mater. *26*, 805–809.